s-PROCESS NUCLEOSYNTHESIS IN ASYMPTOTIC GIANT BRANCH STARS: A TEST FOR STELLAR EVOLUTION

MARIA LUGARO,[1] FALK HERWIG,[2] JOHN C. LATTANZIO,[3] ROBERTO GALLINO,[4] AND OSCAR STRANIERO[5]

ABSTRACT

We study the *slow* neutron capture process (s-process) in asymptotic giant branch (AGB) stars using three different stellar evolutionary models computed for a 3 $M_\odot$, solar metallicity star. First we investigate the formation and the efficiency of the main neutron source: the $^{13}C(\alpha, n)^{16}O$ reaction that occurs in radiative conditions. A tiny region rich in ^{13}C (the ^{13}C *pocket*) is created by proton captures on the abundant ^{12}C in the top layers of the He intershell, the zone between the H shell and the He shell. We parametrically vary the number of protons mixed from the envelope. For high local proton-to-^{12}C number ratios, $p/^{12}C \gtrsim 0.3$, most of the ^{13}C nuclei produced are further converted by proton capture to ^{14}N. Besides, ^{14}N nuclei represent a major neutron poison. We find that a linear relationship exists between the amount of ^{12}C in the He intershell and the maximum value of the time-integrated neutron flux. Then we generate detailed s-process calculations on the basis of stellar evolutionary models constructed with three different codes, all of them self-consistently finding the third dredge-up, although with different efficiency. One of the codes includes a mechanism at each convective boundary that simulates time-dependent hydrodynamic overshoot. This mechanism depends on a free parameter f and results in partial mixing beyond convective boundaries, the most efficient third dredge-up, and the formation of the ^{13}C pocket. For the other two codes, an identical ^{13}C pocket is introduced in the postprocessing nucleosynthesis calculations. The models typically produce enhancements of heavy elements of about 2 orders of magnitude in the He intershell and of up to 1 order of magnitude at the stellar surface, after dilution with the convective envelope, thus generally reproducing spectroscopic observations. The results of the cases without overshoot are remarkably similar, pointing out that the important uncertainty in s-process predictions is the ^{13}C pocket and not the intrinsic differences among different codes when no overshoot mechanism is included. The code including hydrodynamic overshoot at each convective boundary finds that the He intershell convective zone driven by the recurrent thermal instabilities of the He shell (thermal pulses) penetrates the C-O core, producing a He intershell composition near that observed in H-deficient central stars of planetary nebulae. As a result of this intershell dredge-up, the neutron fluxes have a higher efficiency, both during the interpulse periods and within thermal pulses. The s-element distribution is pushed toward the heavier s-process elements, and large abundances of neutron-rich isotopes fed by branching points in the s-process path are produced. Several observational constraints are better matched by the models without overshoot. Our study needs to be extended to different masses and metallicities and in the space of the free overshoot parameter f.

Subject headings: nuclear reactions, nucleosynthesis, abundances — stars: AGB and post-AGB — stars: evolution

1. INTRODUCTION

When helium is exhausted in the center of low-to-intermediate–mass stars ($M \lesssim 8\ M_\odot$), the core becomes degenerate (Paczyński 1970) and burning processes do not occur there anymore. Instead, H and He burn alternately in shells while the star ascends the asymptotic giant branch (AGB). In this phase the stellar structure consists of, from the center outward, a degenerate C-O core, the He-burning shell, a thin (10^{-2} to $10^{-3}\ M_\odot$) zone between the H shell and the He shell (hereafter the He intershell), the H-burning shell, and a

large convective envelope, which suffers from strong stellar winds. When the envelope mass is reduced to less than $\sim 10^{-3}\ M_\odot$, the star leaves the AGB, a planetary nebula is formed, and the C-O core cools toward the white dwarf phase. In 10%–20% of cases, the residual H-rich envelope is completely removed by processes associated with a late He shell instability during the pre–white dwarf phase (Herwig et al. 1999), leading to the formation of the H-deficient central stars of planetary nebulae.

During the AGB, the H shell dominates the energy production for most of the time. Hydrogen is transformed into He, and the He intershell consequently grows and is progressively compressed and heated until the temperature and density become high enough that He burning is triggered in the bottom layers. The thermonuclear runaway, also known as thermal instability, or *thermal pulse* (Schwarzschild & Härm 1965), generated by this sudden release of energy causes almost all the He intershell to become convective (we refer to this as the *pulse-driven convective zone*, hereafter the PDCZ), while the envelope expands and the H shell cools. Within the PDCZ, partial He burning produces large

[1] Institute of Astronomy, University of Cambridge, Madingley Road, Cambridge CB3 0HA, UK; mal@ast.cam.ac.uk.

[2] Department of Physics and Astronomy, University of Victoria, Box 3055, Victoria, BC V8W 3P6, Canada; fherwig@uvastro.phys.uvic.ca.

[3] School of Mathematical Sciences, P.O. Box 28M, Monash University, Victoria 3800, Australia; j.lattanzio@sci.monash.edu.au.

[4] Dipartimento di Fisica Generale, Università di Torino, Via Pietro Giuria 1, 10125 Torino, Italy; gallino@ph.unito.it.

[5] Osservatorio Astronomico di Collurania, Teramo, Italy; straniero@te.astro.it.

amounts of carbon. The PDCZ quenches after a time of a few tens to a few hundreds of years, while He burning continues radiatively for another few thousand years, during which the H shell is inactive. Then the envelope contracts and H shell burning starts again. The cycle is repeated for a few up to possibly 100 times, the total number of thermal pulses depending on the initial stellar mass and the mass-loss rate, with thermal periods of a few times 10^3 up to 10^5 yr. Recent models of the AGB phase have been computed by, among others, Hollowell & Iben (1988), Boothroyd & Sackmann (1988a, 1988b, 1988c, 1988d), Lattanzio (1986, 1987, 1989), Vassiliadis & Wood (1993), Blöcker (1995), Forestini & Charbonnel (1997), Straniero et al. (1997), Wagenhuber & Groenewegen (1998), Mazzitelli, D'Antona, & Ventura (1999), Mowlavi (1999), and Herwig (2000).

As illustrated in Figure 1, after a limited number of thermal pulses, when the mass of the H-exhausted core is above $\sim 0.6\ M_\odot$, the convective envelope penetrates the top layers of the He intershell, bringing to the surface newly synthesized He, C, and elements produced by neutron captures. This recurrent phenomenon is called *third dredge-up* (TDU). The TDU is responsible for the carbon enrichment shown by MS, S, and C(N) stars. Unfortunately, the reproducibility of the TDU phenomenon is a main problem with AGB computations, connected to the more general astrophysical problem of the treatment of turbulent convection in stellar interiors. Different evolutionary codes do not

reproduce the same results: some codes find a large amount of TDU at solar metallicity only for intermediate-mass stars ($5\ M_\odot \lesssim M \lesssim 8\ M_\odot$; Iben 1975a); others find TDU to occur in low-mass stars ($M < 5\ M_\odot$), but only for low metallicities: 1/200 of solar (Iben & Renzini 1982a) and 1/20 of solar (Boothroyd & Sackmann 1988d). Lattanzio (1989) and Straniero et al. (1997) found TDU to occur also in stars with initial mass as low as 1.5 $M_\odot$ and solar metallicity. The amount of TDU is also connected to the evolution of the envelope depending, for example, on the temperature at its base (Wood 1981) and its total mass (Straniero et al. 1997). The inclusion of extra mixing in the computation of TDU, however, can affect these results. The lower limit of 1.5 $M_\odot$ at solar metallicity for TDU to occur is consistent with inferences derived from observational constraints of carbon stars (Groenewegen, van den Hoek, & de Jong 1995). Frost & Lattanzio (1996) studied the effect of the numerical treatment on the occurrence and magnitude of TDU, while Mowlavi (1999) tested the effect of using an extra mixing mechanism at the base of the convective envelope and found that TDU occurs in his models only if this procedure is applied. Recently, Pols & Tout (2001) showed that when the AGB evolution is computed by solving simultaneously the structure equations and the diffusion equations for changes in chemical composition, the TDU strongly depends on numerical choices, such as how the diffusion coefficients are averaged.

Another debated problem is a satisfactory description of mass loss during the AGB phase. It is believed that the main mechanism responsible for mass loss in red giants is radiation pressure on dust grains. Detailed calculations in conjunction with new observations will address this problem. The most recent works include Wachter et al. (2002) and Olofsson et al. (2002). In the past, an often employed way to include mass loss has been to use the Reimers (1975) formula, in which the mass-loss rate depends on the luminosity, radius, and mass of the star and is proportional to a free parameter η, whose value can vary (typically from $\simeq 0.3$ to 10). Other semiempirical relations for the mass-loss rate have been proposed, in particular by Vassiliadis & Wood (1993), Blöcker (1995), and Arndt, Fleischer, & Sedlmayr (1997). Marigo (2002) investigated the effects of molecular opacities on the evolution of AGB stars as the C/O ratio grows from below to above unity and found that in the carbon-rich models, a notable cooling results, and hence, an early onset of the *superwind* is expected in the framework of the Vassiliadis & Wood (1993) formulation of the mass-loss rate.
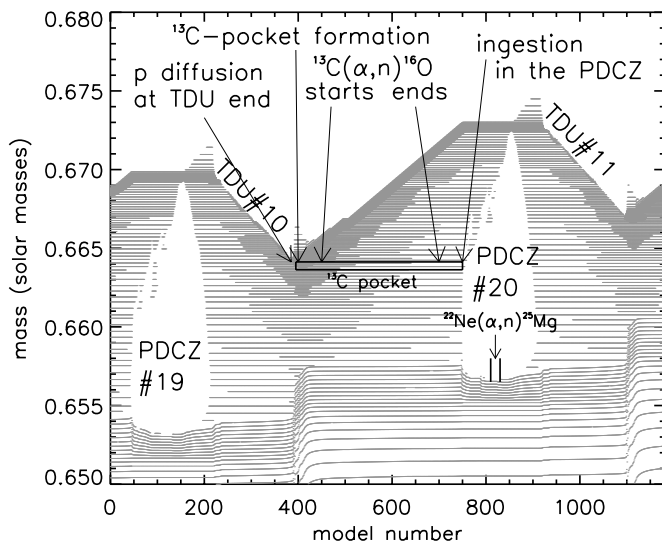

FIG. 1.—Structure evolution through two thermal pulses of a 3 $M_\odot$ star model of solar metallicity, computed with the MSSSP stellar evolutionary code (see § 2). The *y*-axis shows the Lagrangian mass coordinate in solar masses. Convective regions are white, and it is possible to recognize the PDCZs during the 19th and 20th pulses, as well as the bottom of the convective envelope. The gray lines in the radiative regions represent the mass shells. The region with the higher mesh density is the H-burning shell. The ^{13}C pocket is a local phenomenon involving a mass region of the order of half a tick mark (or less) on the *y*-axis. The *x*-axis is a representation of time by model number (from the Monash nucleosynthesis postprocessing code; see § 3). The corresponding approximated time intervals are as follows: starting from $t = 0$ at the end of the 19th PDCZ, the 10th TDU lasts for about 160 yr, the formation of the ^{13}C pocket occurs within $t = 2500$ yr, the ^{13}C(α, n)^{16}O reaction starts at $t = 11,000$ yr, and by $t = 42,000$ yr ^{13}C nuclei are depleted to a number lower than 10^{-6}. The ingestion of the pocket in the PDCZ occurs at $t = 52,000$ yr. The PDCZ lasts for about 40 yr, with about 4 yr during which the bottom temperature is above 2.5×10^8 K and the ^{22}Ne(α, n)^{25}Mg reaction is marginally activated.

1.1. *The s-Process*

The He intershell is the site of the *s*-process, the neutron capture nucleosynthesis that occurs when neutron number densities N_n are of the order of 10^6–10^{11} cm^{-3}. In this range of N_n, when an unstable nucleus is produced along the *s*-process chain of neutron captures, it typically decays rather than capture another neutron (Burbidge et al. 1957). However, for relatively high values of neutron density or temperature, several *branchings* along the *s*-process path are open and neutron-rich nuclei can be produced (Ward, Newman, & Clayton 1976). As a rule of thumb, the *s*-process distribution follows the law $\sigma(A)N_s(A) = \text{constant}$, where $\sigma(A)$ is the neutron capture cross section of nucleus A and $N_s(A)$ its *s*-process abundance by number. This rule is only valid locally because of the presence of the neutron magic nuclei

at $N = 50$, 82, and 126. These nuclei have very low neutron capture cross sections, which make them behave as bottlenecks for the neutron flux. As a consequence, steps in the otherwise $\sigma(A)N_s(A) = $ constant distribution are found in correspondence to neutron magic nuclei. The depth of these steps is a function of the total time-integrated neutron exposure, $\tau = \int_0^t N_n v_T \, dt$ (where v_T is the thermal velocity), so that different neutron exposures lead to different $\sigma(A)N_s(A)$ distributions (see Clayton 1968, p. 568). In AGB stars, heavy *s*-process elements are produced by the *s*-process and then mixed by TDU to the stellar surface, where they have been observed (for general references, see Smith & Lambert 1990; Wallerstein et al. 1997; Wallerstein & Knapp 1998; Busso et al. 2001; Abia et al. 2001). In particular, AGB stars are responsible for the *s*-process *main component* (Käppeler, Beer, & Wisshak 1989; Arlandini et al. 1999; Travaglio et al. 1999), i.e., a significant fraction of the Galactic production of elements from Sr to Pb, as well as for the *strong component* (Clayton & Rassbach 1967) feeding a large fraction of solar ^{208}Pb (Gallino et al. 1998; Goriely & Mowlavi 2000; Travaglio et al. 2001).

The ^{13}C$(\alpha, n)^{16}$O reaction is activated at low temperatures ($\gtrsim 0.8 \times 10^8$ K) and plays the major role as neutron source in AGB stars (Hollowell & Iben 1988; Gallino et al. 1988; Käppeler et al. 1990). However, a higher amount of ^{13}C than is present in the H-burning ashes is needed to reproduce the observed enhancements of heavy elements. To enable the formation of a region rich in ^{13}C, the ^{13}C *pocket*, a few protons from the envelope must penetrate the He intershell and then react with the ^{12}C nuclei abundantly present there. The possibility of penetration of protons from the envelope directly into the convective PDCZ was found by Iben (1976) to be severely inhibited by an entropy barrier induced by the still-active H-burning shell. A favorable location for the mixing of protons is the sharp H/He discontinuity that is left over after the occurrence of TDU while the H shell is temporarily extinguished (Iben & Renzini 1982b). Recently, models including time-dependent overshoot (Herwig et al. 1997), motivated by hydrodynamic simulations by Freytag, Ludwig, & Steffen (1996; see also Singh, Roxburgh, & Chan 1998), and models with rotation (Langer et al. 1999) have been able to create a proton-rich layer with $M_{\text{pocket}} \sim 10^{-5}$ to 10^{-6} $M_\odot$ at the top of the He intershell after the end of the TDU. A similar effect was obtained by imposing a velocity gradient profile beyond the border of the convective envelope (Cristallo et al. 2001). Another description of turbulent perturbation of stable layers below convective zones can be performed in the framework of internal gravity waves (Denissenkov & Tout 2003). In summary, the occurrence of hydrogen penetration at the top of the He intershell seems plausible, but the mass involved and the resulting ^{13}C abundance profile are still to be treated as relatively free parameters, constrained by the rates of proton captures on the carbon isotopes.

The *s*-process mechanism in AGB stars is visualized in Figure 1. After less than a few thousand years, ^{13}C and ^{14}N are produced by proton capture on the abundant ^{12}C in the top layers of the He intershell. Subsequently, after about 10,000 yr, the ^{13}C$(\alpha, n)^{16}$O reaction is activated during the interpulse phase in radiative conditions at a relatively low temperature: $\sim 0.9 \times 10^8$ K (Straniero et al. 1995). Before the end of the interpulse period, all ^{13}C has burnt and the pocket has become enriched in *s*-processed material. This *s*-process nucleosynthesis occurs in radiative conditions;

hence, there is no interaction among the different layers of the pocket. Each zone can be treated separately, and the efficiency of the neutron flux is a local property that only depends on the initial $p/^{12}$C ratio in that layer. The neutron flux lasts typically 20,000 yr and produces locally high neutron exposures, of the order of 10^{-1} mbarn^{-1}. On the other hand, because the timescale is long, the neutron density remains low, reaching about 10^7 cm^{-3}. At the end of the interpulse, the pocket is engulfed by the following PDCZ and mixed with ashes from the H-burning shell and material from the previous PDCZ. A large amount of ^{22}Ne is present in the PDCZ as a product of the chain ^{14}N$(\alpha, \gamma)^{18}$F$(\beta^+, \nu)^{18}$O $(\alpha, \gamma)^{22}$Ne starting on the abundant ^{14}N from the H-burning ashes. In the convective zone, the ^{22}Ne$(\alpha, n)^{25}$Mg reaction can be marginally activated, and a second neutron flux occurs. This second neutron burst is opposite in features to that in the pocket: it occurs on a timescale of a few years, and it produces low neutron exposures (of the order of 10^{-2} mbarn^{-1}) with a high-peaked neutron density, up to 10^{10} cm^{-3}. This neutron burst does not typically contribute much to the overall production of *s*-elements; however, it affects the final abundances of isotopes connected to branching points. For an extensive review on the *s*-process in AGB stars see Busso, Gallino, & Wasserburg (1999).

We want to analyze the dependence of *s*-process model predictions on the stellar evolutionary code used to compute them. We compare the results of postprocessing models based on three evolutionary sequences computed with three different codes, one of them including an overshoot mechanism. The sequences are different in the details of the description of physical processes, such as mass loss, and of the numerical solution scheme adopted. For our purposes, these computations represent a typical set of models of the same star constructed by different groups. The paper is organized as follows: in § 2, we describe the stellar evolutionary codes and the evolutionary sequences we used to compute the nucleosynthesis. In § 3, we describe the nucleosynthesis codes, the formation and efficiency of the ^{13}C neutron source, and the neutron fluxes and final *s*-process distributions as computed with the different evolutionary sequences. In § 4, we compare the final results with a number of observational constraints. In § 5, we outline our conclusions. A preliminary study was presented by Lugaro & Herwig (2001).

2. THE EVOLUTIONARY CODES

To establish the main effects and dependencies, we consider only the case of a star of initial mass 3 $M_\odot$ and solar metallicity. The most recent *s*-process studies (Gallino et al. 1998; Busso et al. 1999; Goriely & Mowlavi 2000) have shown that there is an important variation in the resulting *s*-process distribution with stellar metallicity. The ^{13}C in the pocket is a primary neutron source, having formed from H and the ^{12}C resulting from He burning; hence, for decreasing metallicities heavier and heavier elements are produced, because there are more neutrons per iron seed. This property has been shown to have important consequences in the study of the *s*-process at different metallicities (Busso et al. 2001) and hence on the Galactic chemical evolution of heavy elements (Travaglio et al. 1999). We do not discuss this point to a large extent, since we only consider models of solar metallicity. Busso et al. (2001) demonstrated that a spread in the efficiency of the neutron release in the ^{13}C

pocket is necessary to cover the spectroscopic observations at any given metallicity. Again, we do not discuss this result in detail, because for sake of a simple comparison we perform s-process calculations using a given ^{13}C pocket, chosen as either a relatively free parameter in the evolutionary sequences without overshoot or the result from the computation in the evolutionary sequence with overshoot included.

We consider three different stellar evolutionary codes: the Frascati Raphson-Newton Evolutionary Code (FRANEC; Straniero et al. 1997), the Mount Stromlo Stellar Structure Program (MSSSP; Wood & Zarro 1981; Frost & Lattanzio 1996), and the EVOL code (Blöcker 1995; Herwig 2000). Since the codes are independent, they contain several differences, e.g., with respect to the numerical treatment, opacities, and nuclear reaction rates. The most important difference to be noted here, however, is the treatment of convective instabilities and the associated mixing, which influence the calculation of the TDU phenomenon and the formation of the ^{13}C pocket.

In the framework of the mixing-length theory, mixing velocities should drop to zero at the boundary of a convective layer, where the radiative temperature gradient ∇_{rad} equals the adiabatic temperature gradient ∇_{ad}, $\nabla_{rad} - \nabla_{ad} = 0$, defining the Schwarzschild boundary. In reality, because of inertia, convective eddies are more likely to have nonzero velocity and to be dragged across the Schwarzschild boundary. This idea is the basis of the concept of mechanical overshoot. However, when convection penetrates a chemically inhomogeneous region, a discontinuity in the opacity forms at the stability border. When the opacity in the convective region is larger than the opacity in the radiative region, then $\nabla_{rad} - \nabla_{ad} > 0$ at the convective border seen from the radiative zone. In this condition extra mixing is induced by the change of composition, and this causes the border to advance into the radiative zone. A famous example of such a situation is found at the outer border of the convective core during central He burning: the opacity increases, because of the conversion of He into C and O, and the convective region grows in mass (Paczyński 1970; Castellani, Giannone, & Renzini 1971). The same phenomenon is encountered during the TDU phases (Becker & Iben 1979; Castellani, Chieffi, & Straniero 1990): the H-rich convective envelope penetrates the He-rich intershell layer, which has a substantially lower opacity.

To handle this special condition in AGB models, the MSSSP code uses a numerical scheme that may involve mixing of an additional stable mass shell after each structure iteration: " Suppose mesh point j is the outer (inner) edge of a formally convective zone. By evaluating the radiative to adiabatic ratio ∇_{rad}/∇_{ad} at mesh point $j - 1$ ($j + 1$), we can extrapolate to find $(\nabla_{rad}/\nabla_{ad})_{extrap}$ at $j + 1$ ($j - 1$). If this value is greater than unity, then we incorporate the $j + 1$ ($j - 1$) mass shell into the convective zone, even though the shell may have $\nabla_{rad} < \nabla_{ad}$ when calculated formally. This procedure is executed, at each convective boundary, each time the abundances are mixed over a convective region " (Lattanzio 1986). Note that in the MSSSP code convective regions are mixed after each structure iteration. A further modification to MSSSP was described by Frost & Lattanzio (1996) to allow for the case in which the increasing depth of the convective envelope (with each iteration) was followed by a retreat of the envelope convection, leading to failure to converge. When this occurs, the iterations are treated as

capturing the essential time-dependent response of the structure to the induced mixing. Hence, the greatest depth of the convective envelope is taken as the mixed region, which cannot later be unmixed during subsequent iterations for this model. This mixed abundance is taken as the composition for subsequent iterations, perhaps leading to convergence with a shallower *convective* zone but with the deeper *mixed* region.

No special algorithms are adopted by the FRANEC code version used here to handle the discontinuity in the chemical composition and the consequent jump of the opacity that forms at the base of the convective envelope. Since both MSSSP and FRANEC assume instantaneous (homogeneous) mixing, neither of them can find the proton mixing into the He intershell at the end of TDU needed for the formation of a ^{13}C pocket. The main difference between the two codes is the amount of TDU mass, which is higher in the MSSSP case.

In EVOL a time- and depth-dependent overshoot mechanism is included at the convective borders within the star, which induces partial mixing beyond the boundary of homogeneously mixed regions. This scheme mimics mixing because of an exponential decay in space of the convective velocity field into the stable layers, as observed in hydrodynamic simulations, following the prescription of Freytag et al. (1996), who performed two-dimensional hydrodynamic simulations of time-dependent compressible convection in order to study shallow stellar surface convection zones. A similar behavior of the decay of the convective velocity field outside the convection zone has been found by Asida & Arnett (2000) in two-dimensional hydrodynamic simulations of the oxygen-burning shell in massive stars. The scale height of these types of mixing remains a free parameter (f) for the convective boundaries considered here. This type of hydrodynamical overshoot has also been used by Mazzitelli et al. (1999) and Schlattl & Weiss (1999).

Herwig (2000) showed that this algorithm, when applied to thermally pulsing AGB models, is relevant to address some major observational properties. Time-dependent hydrodynamic overshoot is a process that naturally leads to the formation of the ^{13}C pocket needed for the occurrence of the s-process over a range of 10^{-6} to 10^{-5} $M_\odot$. It increases the TDU efficiency and therefore may better account for low-luminosity carbon stars (Herwig, Blöcker, & Driebe 2000). It leads to intershell dredge-up of C-O core material in the helium intershell. This enhances the C and O intershell abundances, as required by models, such as those presented by Herwig et al. (1999), that reproduce observations of hot, H-deficient, post-AGB stars of type PG 1159 (Dreizler & Heber 1998) and central stars of planetary nebulae of spectral type WC (Leuenhagen & Hamann 1998). All these effects depend on the value of a free overshoot parameter f. Here we want to check whether the inclusion of hydrodynamic overshoot is in contradiction with other observational information, in particular that connected with the activation of the neutron sources and the consequent s-process nucleosynthesis. We use a value of $f = 0.016$ at every convective boundary, except at the base of the convective envelope, where we use $f = 0.128$ for the computation of the ^{13}C pocket. The original value of 0.016 was chosen to model main-sequence core overshoot in order to reproduce the observed width of the main sequence (Schaller et al. 1992). However, with this choice the mass of the ^{13}C pocket, and consequently the total mass of s-process material, is too

small to account for observations (as already pointed out by Goriely & Mowlavi 2000).

Cristallo et al. (2001) also find partial mixing of protons below the base of the convective envelope with the FRANEC code. They achieve this by means of a time-dependent mixing scheme (see Chieffi et al. 2001), with mixing velocities derived in the framework of the mixing-length theory. To handle the $\nabla_{\rm rad} - \nabla_{\rm ad}$ discontinuity condition during TDU, Cristallo et al. (2001) assume that the mixing velocity drops to zero below the Schwarzschild boundary of the convective envelope, with an exponential decline in space. This choice induces both a deeper TDU and the formation of a tail of the internal H profile, thus allowing the subsequent formation of the ^{13}C pocket. Also in this case, the efficiency of the TDU and the extension of the resulting ^{13}C pocket depend on the efficiency of the assumed exponential decline of the velocity field, i.e., a free overshoot parameter f_v. The main difference with respect to the scheme adopted by EVOL is that in Cristallo et al. (2001), the overshoot is induced only where there is a $\nabla_{\rm rad} - \nabla_{\rm ad}$ discontinuity, i.e., at the base of the convective envelope during TDU. We also briefly comment on the s-process results obtained by using as inputs the ^{13}C pocket and the stellar features of the FRANEC stellar model of 3 $M_\odot$ and solar metallicity with the Reimers (1975) parameter $\eta = 1.5$ and overshoot parameter $f_v = 0.1$ presented by Cristallo et al. (2001). This computation was followed for 17 pulses with TDUs, resulting in a final envelope mass of 1.3 $M_\odot$. Because of the algorithm of overshoot included at the base of the convective envelope, the dredge-up mass is higher than in the FRANEC standard case, reaching up a total of 0.06 $M_\odot$, and C/O is above unity in the last five pulses. The ^{13}C pocket was found to form over a mass of about 4×10^{-4} $M_\odot$.

Mass loss has also been modeled in different ways: the FRANEC code uses the Reimers (1975) prescription with $\eta = 1.5$ throughout the whole evolution; the MSSSP evolution has been computed with the Reimers (1975) mass loss with $\eta = 1$ until the beginning of the AGB phase and afterward using the formula proposed by Vassiliadis & Wood (1993), which accounts for a superwind phase. The EVOL code uses the Reimers (1975) mass loss with $\eta = 1$ from the pre–main sequence to the point where C/O = 1 in the envelope. Afterward, it uses the Arndt et al. (1997) rate for carbon stars.

2.1. The Stellar Evolutionary Sequences

We computed s-process detailed nucleosynthesis for a stellar model of 3 $M_\odot$ and solar metallicity, making use of the structural, thermodynamical, and chemical characteristics obtained from the three different evolutionary codes described above. The FRANEC sequence ends because of convergence problems after 25 thermal pulses with TDU, when TDU is vanishing because of the low envelope mass; the MSSSP sequence also stops for convergence problems after 18 pulses with TDUs, with an envelope mass similar to that of the FRANEC case. For the EVOL sequence, the adopted mass-loss law results in a low mass-loss rate. After reaching the 13th TDU we stopped the sequence, under the assumption that an efficient superwind phase will remove the remaining envelope within a few thermal pulses.

In Figure 2, we present some quantities related to the evolution of the convective envelope during the AGB phase as functions of the mass of the H-exhausted core $M_{\rm H}$: the mass

dredged up by each TDU episode, the cumulative mass dredged up by all previous TDU episodes, the mass of the envelope, and the C/O ratio in the envelope. Each point corresponds to a thermal pulse followed by TDU. The dredged-up mass and the envelope mass are determined by the different choices made in each code described above. Because of the different mixing algorithms and assumptions on overshoot, the amount of dredged-up mass grows from FRANEC, which does not include any treatment of the discontinuity of the adiabatic-to-radiative gradient ratio at the base of the convective envelope, to MSSSP, which attempts to find the neutrality in that ratio, to EVOL, which includes an algorithm for hydrodynamic overshoot. For the three models, TDU starts after the ninth, tenth, and first thermal pulse, respectively, when the core mass has reached $\simeq 0.61$–0.63 $M_\odot$. The AGB sequence with EVOL starts with a larger core mass because of overshoot during the main sequence. In the 3 $M_\odot$ model presented by Herwig (2000), the TDU starts at the fourth pulse. The difference is due to the different value of f applied at the base of the convective envelope. An interesting consequence of the deep TDU experienced by the EVOL model is that after the first six pulses the core mass does not grow anymore; rather, it decreases with time (Herwig, Schönberner, & Blöcker 1998).

The evolution of the envelope mass is determined by the choice of the mass-loss law. For FRANEC, the Reimers (1975) formula determines a continuous decrease of the envelope mass; for MSSSP, which uses the Vassiliadis & Wood (1993) mass-loss law, the mass of the envelope is kept quite constant until a superwind sets in during the last two pulses. In EVOL, which uses Reimers (1975) for the first six pulses and then Arndt et al. (1997) when the envelope is carbon-rich, the mass loss is not as large as in the FRANEC and MSSSP cases, and the envelope mass is about double that in the other two cases right to the end of the computed evolution. The C/O ratio at each pulse is determined by the mass dredged up and the envelope mass, and also by the C and O abundances in the intershell, which are both larger in the EVOL case because of intershell dredge-up. All the models become carbon-rich in the envelope after a given number of dredge-up events.

In Figure 3, we compare some interesting features of the He intershell as functions of the core mass: the interpulse period, the extent in mass of the intershell convective region, the overlap factor r between subsequent pulses, and the bottom temperature of the PDCZ. On this last quantity depends the activation of the ^{22}Ne neutron source. While in the FRANEC and MSSSP cases the interpulse period decreases with time and is very similar to previous AGB models (such as those presented by Boothroyd & Sackmann 1988c), in the EVOL case the interpulse period increases with time from $\sim$60,000 to $\sim$80,000 yr. This difference is a consequence of the fact that in EVOL the core mass decreases with time, since the lower the core mass, the larger the interpulse period (Paczyński 1974). For the three stellar evolutionary codes examined, the mass of the PDCZ decreases with time and is higher in the EVOL case because the convection extends down into the C-O core. The overlap factor r decreases with time in all cases. The decrease is steeper for cases with larger TDU. The maximum temperature at the base of the PDCZ grows with the pulse number in all three cases. The FRANEC trends are very close to those of Boothroyd & Sackmann (1988c). In EVOL the maximum temperature reached is 3.20×10^8 K, compared
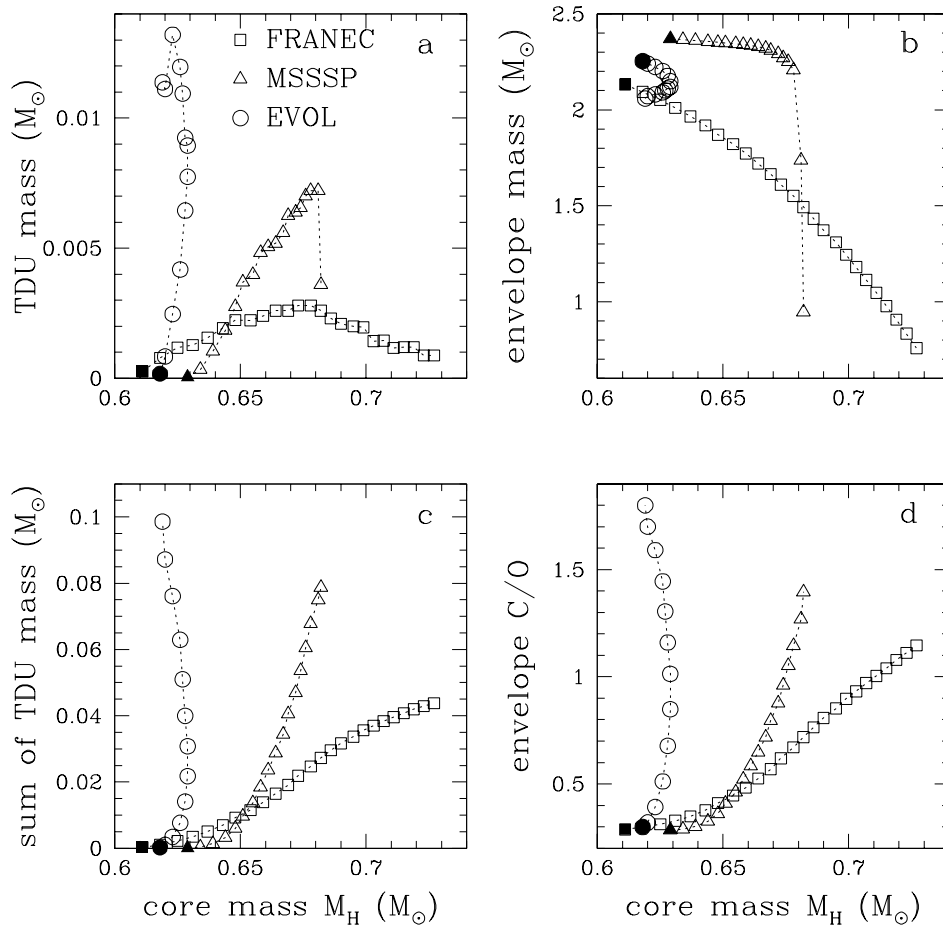
Fig. 2.—TDU mass and envelope features as functions of the mass of the H-exhausted core for the 3 $M_\odot$ and solar metallicity models computed with the FRANEC (*open squares*), MSSSP (*open triangles*), and EVOL (*open circles*) codes. Each point corresponds to a thermal pulse followed by the TDU. These models were used to compute the *s*-process. For each sequence the filled symbol represents the starting point from which the evolution develops, following the dotted lines connecting the open symbols. Note that the core mass always increases with time in the FRANEC and MSSSP cases, while in the EVOL case it decreases with time after six pulses. For each model we show: (*a*) the mass dredged up by each single TDU episode, (*b*) the envelope mass, (*c*) the cumulative mass dredged up, and (*d*) the C/O ratio in the envelope.

to the maximum value of 3.05×10^8 K reached in the FRA-NEC and MSSSP case. This higher temperature is a consequence of the hydrodynamical overshoot applied at the base of the intershell convection zone.

3. THE NUCLEOSYNTHESIS CALCULATIONS

We have used two different postprocessing nucleosynthesis codes for different aims. To investigate the formation of the ^{13}C pocket and evaluate the efficiency of the ^{13}C main neutron source, we have made use of the Monash nucleosynthesis code; to perform detailed *s*-process calculations we have used the *s*-process code by Gallino et al. (1998).

The Monash nucleosynthesis code reads a file of stellar structure inputs, such as temperature and density, that is produced by the MSSSP evolutionary code. The nuclear network is specifically designed for the detailed study of light-element nucleosynthesis in AGB stars. In the nucleosynthesis network there are 74 nuclear species. From neutrons and protons up to sulphur there are 59 nuclei, with another 14 iron-group species to allow neutron capture on iron seeds; there is also an additional "particle" g, which has the function of counting the number of neutron captures occurring beyond ^{60}Ni, hence giving an estimation of the

resulting heavier elements' *s*-process distribution. All proton, α, and neutron captures and β-decays involving the species listed above are included in the nuclear network, summing up to 506 reactions. The bulk of reaction rates are from the Reaclib Data Tables of nuclear reaction rates based on the 1991 updated version of the compilation by Thielemann, Arnould, & Truran (1987). They have been updated to the latest new experimental or theoretical estimates (Lugaro 1998). The reaction network is terminated by a neutron capture on ^{61}Ni followed by an ad hoc decay with $\lambda = 1$ s^{-1}, producing the particle represented by the symbol g: ^{61}Ni$(n, \gamma)^{62}$Ni$\rightarrow^{61}$Ni$+g$. The Q-value assigned to this reaction is the value of the reverse reaction ^{62}Ni$(\gamma, n)^{61}$Ni. Following the method of Jorissen & Arnould (1989), neutron captures on the missing nuclides are modeled by neutron *sinks*, meaning that the ^{34}S$(n, \gamma)^{35}$S and ^{61}Ni$(n, \gamma)^{62}$Ni reactions are given some averaged cross section values in order to represent all nuclei from ^{34}S to ^{55}Mn and from ^{61}Ni to ^{209}Bi, respectively. We obtained $\sigma(^{34}$S$)_{\rm sink}=$ 21.1 mbarn at 8 keV (the typical temperature of ^{13}C burning), using a solar distribution for the abundances of nuclei from ^{34}S to ^{55}Mn. To compute $\sigma(^{61}$Ni$)_{\rm sink}$, we used different abundance distributions of heavy elements, computed in different phases of the *s*-process in AGB stars of 3 $M_\odot$ and
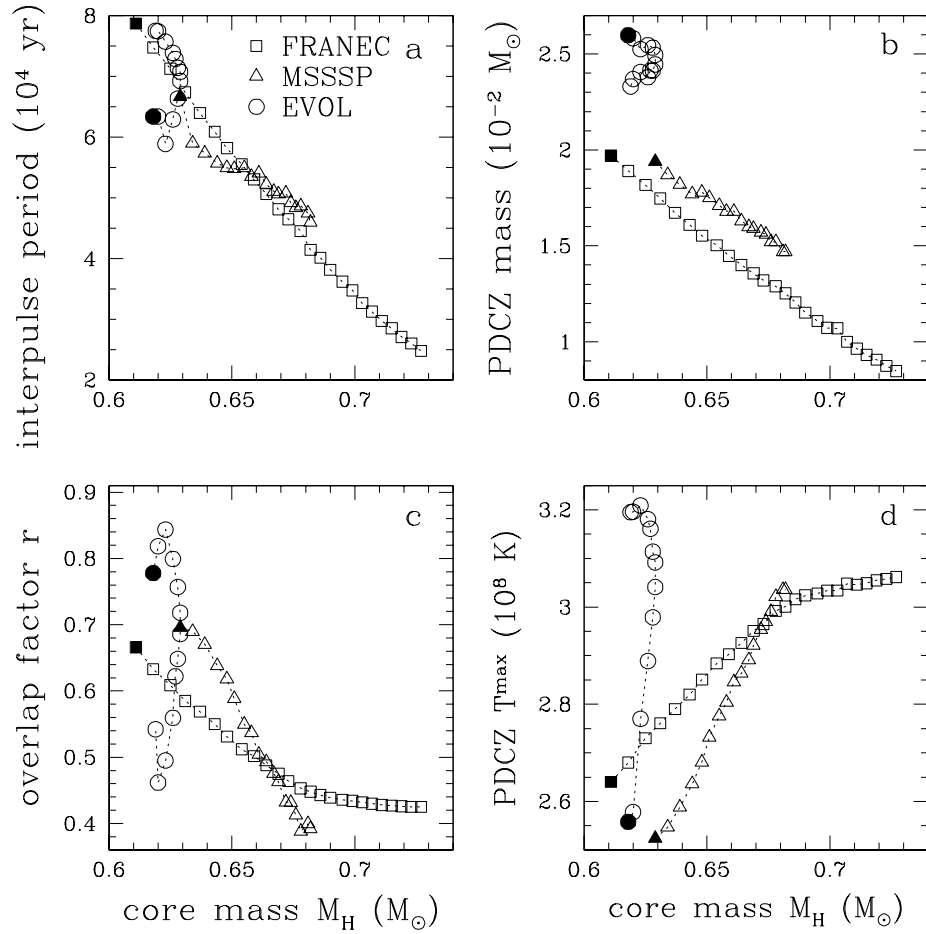
Fig. 3.—Structural and thermodynamical characteristics as functions of the core mass. Each point corresponds to a thermal pulse followed by the TDU. Symbols as in Fig. 2. (*a*) The interpulse period; note that in the EVOL case, the interpulse period increases with the pulse number, while for FRANEC and MSSSP it decreases. (*b*) Mass of the PDCZ, which decreases with time in all cases. (*c*) Overlap factor *r* between subsequent PDCZs, which decreases with time in all cases. (*d*) Variation of the maximum temperature at the bottom of the PDCZs, which increases with time in all cases.

solar metallicity from the models of Gallino et al. (1998). We found that the results do not vary much, changing by up to 15% for different distributions. Therefore, we decided to use as typical the average of such values: $\sigma(^{61}\mathrm{Ni})_{\mathrm{sink}} = 135$ mbarn at 8 keV. For stellar models of different masses or metallicity, this parameter might have to be adjusted. The temporal variation of the neutron density is determined in each layer by the local equilibrium between neutron production and destruction.

The *s*-process code follows a complete set of neutron captures on 404 nuclei from ^{4}He up to Po, where the *s*-process path ends because this element is unstable against α-decay. The α-capture reactions are considered on light nuclei up to Mg. This code uses structure and thermodynamic inputs from computed stellar sequences. Reaction rates for neutron production have been taken, as in the Monash nucleosynthesis code, from Denker et al. (1995) for the ^{13}C(α, n)^{16}O reaction and from Käppeler et al. (1994) for the ^{22}Ne(α, n)^{25}Mg reaction, excluding the contribution of the elusive resonance at 633 keV and using the lower experimental limit for the resonance at 828 keV. Rates for (n, γ) reactions are updated to the latest estimates (Bao et al. 2000; Reifarth et al. 2001; Mutti et al. 2002). Rates for (n, α) and (n, p) reactions are taken from the same sources as in the Monash nucleosynthesis code. Decay rates are mainly from Takahashi & Yokoi (1987).

3.1. *The Formation and the Evolution of the ^{13}C Pocket*

With the Monash nucleosynthesis code we have studied the formation of the ^{13}C pocket and the activation of the ^{13}C(α, n)^{16}O neutron source reaction during a typical interpulse period. This is done to understand the effect of the ^{14}N(n, p)^{14}C neutron poison reaction and the subsequent recycling of protons by the ^{12}C(p, γ)^{13}C reaction, possibly inhibited by the ^{13}C(p, γ)^{13}N reaction and proton captures on other isotopes, such as ^{18}O. We perform the calculations with the Monash nucleosynthesis code because it includes proton captures, while the *s*-process code does not. We derive the main general features of the neutron flux in the ^{13}C pocket and their dependence on various parameters.

We generated the ^{13}C pocket by introducing in the post-processing Monash nucleosynthesis code computation a certain number of protons below the H/He discontinuity at the end of the 10th TDU episode, which follows the 19th thermal pulse in the 3 $M_\odot$ model computed with MSSSP. The initial mass fraction of ^{12}C in the He intershell is $X_{\mathrm{C12}} = 0.23$,[6] which is a very typical value for an advanced PDCZ (see, e.g., Fig. 9 of Boothroyd & Sackmann 1988c).

---

[6] We indicate the mass fraction X of isotope ^{12}C with the notation X_{C12} and use the equivalent for all the other isotopes.

No ^{13}C or ^{14}N from H-burning ashes is present initially in the He intershell, since they have been destroyed by α captures during the previous PDCZ. We performed one-zone model calculations by introducing a constant mass fraction of protons X_p^{init} for each simulation in a region of about $10^{-4}\,M_\odot$. The typical temperature of the top layer of the He intershell grows from about 2×10^7 to about 4.5×10^7 K in the $\simeq 2000$ yr following the end of the TDU. At 4.5×10^7 K, the lifetime of protons with respect to the ^{12}C$(p, \gamma)^{13}$N reaction is less than 200 yr, so that all protons are captured before the onset of H-shell burning, which occurs $\simeq 3000$ yr after the end of TDU. ^{13}C is formed by proton capture on ^{12}C, and ^{14}N is produced by proton captures on the newly formed ^{13}C. The number of protons available determines the ^{13}C and ^{14}N final concentrations. For the ^{12}C$(p,\gamma)^{13}$N reaction we used the rate from Caughlan & Fowler (1988); for the rate of the ^{13}C$(p, \gamma)^{14}$N reaction we used the new evaluation from King et al. (1994), which in this range of temperature is 1.29 times higher than the previous evaluation by Caughlan & Fowler (1988).

The results of these computations are presented in Figure 4. As first shown by Hollowell & Iben (1988) and discussed in detail by Jorissen & Arnould (1989) and Goriely & Mowlavi (2000), for $p/^{12}$C $< 1/10$, the number of ^{13}C nuclei produced is essentially determined by the number of initial protons. Then, for increasing number of protons an increasing fraction of the ^{13}C nuclei suffer a second proton capture and are transmuted to ^{14}N, until, at $p/^{12}$C > 1, a ^{14}N pocket emerges next to the ^{13}C pocket. For $X_p^{\text{init}} \geq 0.02$, $p/^{12}$C ≥ 1 and ^{12}C is strongly depleted, being transformed into ^{14}N. Since ^{14}N is a strong neutron absorber, the region of the pocket that is more efficient for the production of s-process nuclei is where ^{13}C is more abundant than ^{14}N. The results

are affected by the choice of the ^{13}C$(p, \gamma)^{14}$N rate; when the lower rate from Caughlan & Fowler (1988) is used, the final amount of ^{13}C is higher. For example, at $X_p^{\text{init}} = 0.003$, with the older rate we obtain 12% more ^{13}C and 21% less ^{14}N.

The ^{13}C$(\alpha, n)^{16}$O reaction occurs during the interpulse period because the temperature in the ^{13}C pocket layers reaches $\sim 10^8$ K before the start of the next pulse. The lifetime of ^{13}C with respect to the ^{13}C$(\alpha, n)^{16}$O reaction is about 400 yr at this temperature. Thus, ^{13}C is totally destroyed before the onset of the next thermal pulse. With the MSSSP code the temperature in the ^{13}C pocket reaches 10^8 K after about 43,000 yr (with $\rho \sim 13,000$ g cm^{-3} and $X_{\text{He4}} = 0.72$) from the beginning of the interpulse period. The whole interpulse period lasts for about 52,000 yr. Thus, we concur with Straniero et al. (1995, 1997) that all the ^{13}C present in the pocket burns in radiative conditions. (However, it has to be noted that this might not occur during the earliest interpulse periods; see, e.g., Fig. 4 of Herwig 2000.) The resulting neutron exposure is shown in Figure 4. A most important point is the role played by the ^{14}N$(n, p)^{14}$C reaction and the subsequent partial proton recycling (see also Gallino et al. 1998 and references therein). ^{14}N nuclei indeed act as a strong neutron poison during the s-process because of the relatively high cross sections of the ^{14}N$(n, p)^{14}$C reaction: recent measurements give a Maxwellian average cross section of 2.04 ± 0.16 mbarn at 24.5 keV (Gledenov et al. 1995) with a very nearly $1/v$ shape. Neutron capture cross sections of all the other CNO nuclei are typically smaller by about 2 orders of magnitude. The protons produced by this reaction are recaptured by either the abundant ^{12}C, producing ^{13}C again, or the ^{13}C itself, which has a proton capture rate about 10 times larger than that of ^{12}C. The overall effect can be considered as a partial recycling of neutrons together with a leaking of the neutron source. In no case is the proton recycling mechanism efficient enough to leave any ^{13}C present in the pocket at the end of interpulse period. When the mass fraction of ^{14}N is smaller than that of ^{13}C, few neutrons are captured by ^{14}N, and the s-process efficiency is high. In this situation the small recycling effect produces slightly larger final neutron exposures (e.g., 10% higher for an initial proton number of 0.001) than in the test case, when proton captures on ^{12}C and ^{13}C are switched off. When the mass fraction of ^{14}N is higher than that of ^{13}C, most neutrons are captured by ^{14}N to be transmuted into protons. In this situation the recycling effect produces larger final neutron exposures than if proton captures on ^{12}C and ^{13}C were not included (e.g., 30% more for an initial proton number of 0.02). However, the s-process efficiency is low. For $X_p^{\text{init}} > 0.02$, the abundance of ^{12}C, and hence the recycling effect, is much reduced and the neutron flux is unimportant. This explains why, in Figure 4, the total neutron exposure in the ^{13}C pocket reaches a maximum and then decreases as a function of X_p^{init}. In particular, we found that a maximum τ of 0.43 mbarn^{-1} can be achieved, for solar metallicity stars, when X_p^{init} is 0.003 (as also found by Goriely & Mowlavi 2000). In view of this, the highest neutron exposure of 0.44 mbarn^{-1}, reached among the three representative layers of the ^{13}C pocket assumed in Gallino et al. (1998; see their Fig. 6), has to be considered as the maximum allowed for stars of solar metallicity when the mass fraction of ^{12}C in the He intershell $X_{\text{C12}}^{\text{intershell}} \simeq 0.23$.

The recycling/leaking effect is affected by the choice of the ^{13}C$(p, \gamma)^{14}$N rate. When the lower rate from Caughlan & Fowler (1988) is used, ^{13}C is less destroyed by proton
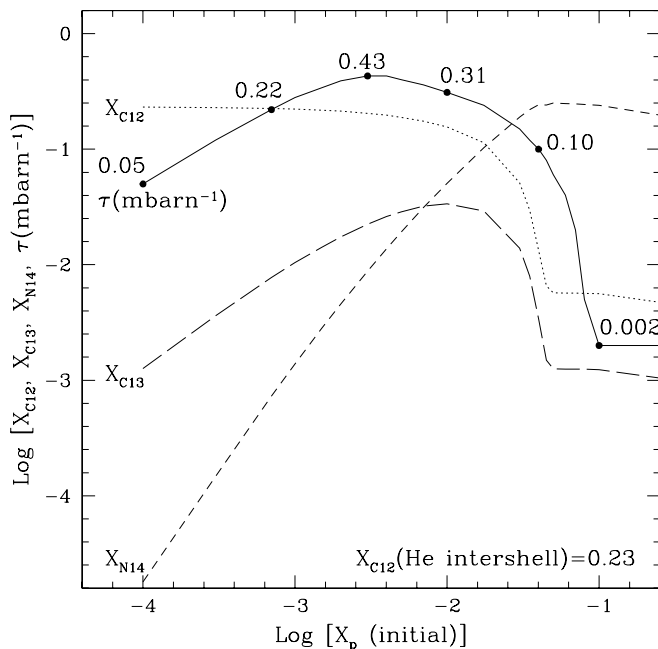

Fig. 4.—Resulting mass fractions of ^{12}C, ^{13}C, and ^{14}N as functions of the initial mass fraction of protons introduced below the H/He discontinuity during the simulations performed with the Monash nucleosynthesis code. The protons are introduced after the 10th TDU episode of the 3 $M_\odot$ star of solar metallicity computed with the MSSSP code. Also plotted is the corresponding neutron exposure at the end of the interpulse period after all the ^{13}C has burnt.

captures. For example, at $X_p^{\text{init}} = 0.003$, with the lower rate we obtain an increase of the value of τ by 18%.

As mentioned in the introduction, for AGB stars of metallicity lower than solar the s-process efficiency is higher for the same initial ^{13}C amount. This is because there are fewer iron nucleus seeds per neutron and fewer light isotopes to act as neutron poisons. However, as well as ^{13}C, the ^{14}N nuclei in the pocket are also of primary origin; i.e., they do not depend on the stellar metallicity, but are produced starting only from the H and He originally present in the star. Hence, the effect of the ^{14}N neutron poison will also be important in stars of lower metallicity, and detailed computations are needed to address this point. Also, rotation could affect the neutron exposure, because in this case mixing continues after H-burning reignition and ^{14}N is mixed down into the ^{13}C-rich region during the interpulse period. This has the effect of strongly lowering the neutron exposure (Herwig, Langer, & Lugaro 2002).

We conducted other simulations in the same 19th interpulse period by artificially changing the intershell amount of ^{12}C. As shown in Figure 5, a nearly linear relationship exists between the final maximum value of τ in the pocket and the intershell ^{12}C, because the latter determines the ^{13}C and ^{14}N profiles and how many protons are recycled. The mass fraction of ^{12}C in the intershell varies from pulse to pulse (see, e.g., Fig. 6 of Schönberner 1979 and Fig. 9 of Boothroyd & Sackmann 1988c), but it typically reaches a constant value around 0.20–0.25 for the advanced pulses where the TDU occurs in the FRANEC and MSSSP computations, while X_{O16} is only $\simeq 0.005$. In the EVOL case, instead, when hydrodynamic overshoot is included and intershell dredge-up is at work, the intershell mass fraction of ^{12}C varies from 0.30 to about 0.50 and then decreases toward an asymptotic value around 0.40. The intershell

mass fraction of ^{16}O increases to about 0.20 and then decreases toward about 0.15 (see Fig. 11 of Herwig 2000). The maximum neutron exposure in the pocket will then vary from pulse to pulse following the ^{12}C abundance.

We have determined here that, given the reaction rates of proton and neutron captures on ^{12}C, ^{13}C and ^{14}N, for a given metallicity and a given intershell abundance of ^{12}C there is a maximum value of the neutron exposure achievable in the pocket, and hence a possible variation of neutron exposure is allowed to be in the range where $\tau < \tau_{\text{max}}$. At solar metallicity, the maximum s-process efficiency is comparable to the maximum value used by Busso et al. (2001) with FRANEC to explain the spread of neutron exposures required by spectroscopic observation.

3.2. The Choice of the ^{13}C Pocket for the s-Process Computations

To follow the ^{13}C pocket with the s-process code, we divided the ^{13}C-rich layer at the envelope-core interface into a number of zones of suitable mass and neutron exposure. The nucleosynthesis in each of these zones is computed individually until the end of the interpulse period. The resulting final abundances in the pocket are obtained as $X_i^{\text{final}} = \left(\sum X_i^{\text{zone}} M_{\text{zone}}\right) / \sum M_{\text{zone}}$, where X_i^{zone} is the final abundance of the isotope i in each zone, M_{zone} the mass of each zone, and the sum is done over all the zones.

To specify the actual ^{13}C pocket profile to run the s-process code with the structure computed by FRANEC and MSSSP, an initial H profile needs to be chosen that relates the X_p x-axis in Figure 4 to the Lagrangian mass coordinate. The extent in mass of the pocket and of each of its zones has to be considered as a free parameter in these computations, thus leaving open the question of the specific shape of the H profile and the mixing processes that lead to the partial mixing. We follow the approach of Gallino et al. (1998) and take the same profile that is plotted in their Figure 1. The total mass for the pocket is $5 \times 10^{-4} M_\odot$, only the region of the pocket where the ^{14}N abundance is lower than the ^{13}C abundance, and hence the s-process is efficient, is considered and more mass is given to the zone characterized by the lower neutron exposures. The ^{13}C profile is kept the same for each cycle; however, as discussed by Gallino et al. (1998; see their Fig. 6), the neutron exposure slightly decreases with the interpulse number. This is because the initial composition of the s-processed material in the ^{13}C pocket is different because of the interplay of the different phases through the whole evolution.

For the EVOL case, we used the ^{13}C pocket self-consistently computed at the fifth interpulse period with the overshoot parameter $f = 0.128$. The initial amount of ^{12}C, ^{13}C, and ^{14}N, together with the resulting final neutron exposure as functions of the position in mass, are plotted in Figure 6. The total mass of the pocket is $3.7 \times 10^{-5} M_\odot$. As noted in the previous section, the higher the initial ^{12}C amount, the higher is the maximum τ allowed (see Fig. 5). Because of intershell dredge-up, the intershell mass fraction of ^{12}C found with the EVOL code, at this interpulse, is 0.48. The maximum of the neutron exposure is 0.84 mbarn^{-1}, double the value obtained with the FRANEC and MSSSP codes, for which $X_{\text{C12}}^{\text{intershell}} \simeq 0.23$. We note that this maximum neutron exposure is about 20% higher than the value of 0.70 mbarn^{-1} obtained with the tests presented in § 3.1 and shown in Figure 5 for the same ^{12}C abundance in the He
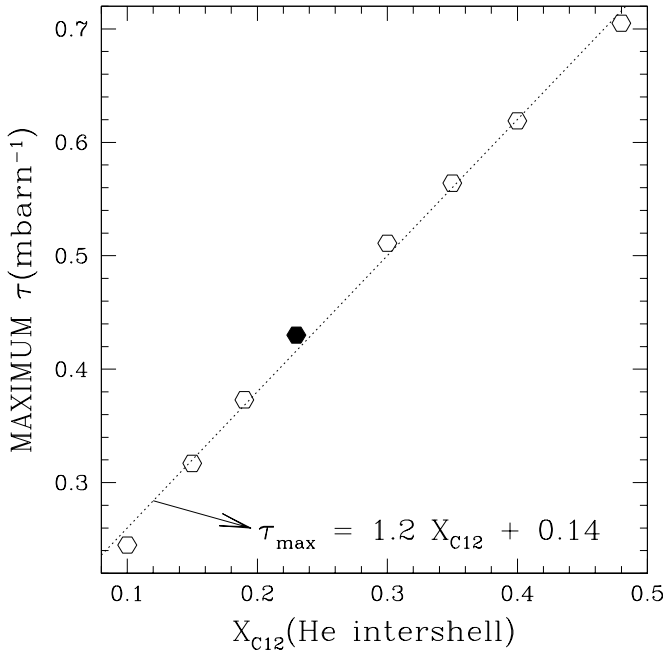

FIG. 5.—Maximum neutron exposure in the pocket as a function of the He intershell ^{12}C, from the simulations performed at the 10th TDU episode of the 3 $M_\odot$ model of solar metallicity computed with the MSSSP code. The filled hexagon indicates the true $X_{\text{C12}}^{\text{intershell}}$ value at such interpulse resulting with MSSSP.
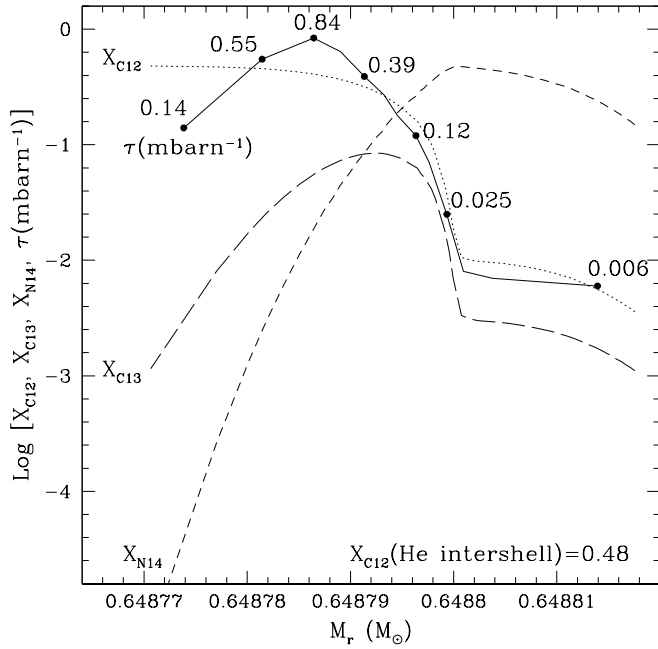
$$\tau_{\text{max}} = 1.2 \, X_{\text{C12}} + 0.14$$

FIG. 6.—Abundance profiles in the ^{13}C pocket found self-consistently by the EVOL code at the fifth interpulse period with the overshoot parameter $f = 0.128$. The large tick marks on the x-axis measure 10^{-5} $M_\odot$ intervals. Also shown is the resulting τ at the end of the interpulse, as subsequently computed by representing the abundance profiles with 10 zones and performing one-zone computations with the Monash nucleosynthesis code.

FIG. 7.—(a) Temperature from the three evolutionary codes and (b) neutron density as computed by the s-process code in zone 3 of the ^{13}C pocket with the higher neutron density. The zero points in time represent the time from the start of the interpulse period, about 10,000 yr, when in the MSSSP case $T = 0.79 \times 10^8$ K. Matter densities also grow with time from $\simeq 2 \times 10^3$ to 10^4 g cm^{-3} for FRANEC and EVOL and to $\simeq 1.5 \times 10^4$ g cm^{-3} for MSSSP.

intershell. This is due to the fact that the profiles of Figure 6 have been obtained using the ^{12}C$(p,\gamma)^{13}$N reaction rate from Caughlan & Fowler (1988), which, as already shown in § 3.1, produces a small increase in the neutron exposure.

3.3. The Neutron Flux in the ^{13}C Pocket

To compare the neutron fluxes in the interpulse period as obtained with the three different evolutionary sequences, we plot in Figure 7 the temperature from the three stellar evolution calculations for a typical interpulse period and the resulting neutron density as computed by the s-process code in the layer of the pocket characterized by the higher neutron density. For FRANEC and MSSSP, the temperature shown corresponds to a point in mass at about 3.3×10^{-4} $M_\odot$ below the H/He discontinuity left by the TDU, for the EVOL code it corresponds to the point of the maximum of ^{13}C in the pocket, which is located at about 3×10^{-5} $M_\odot$ below the H/He discontinuity left by the TDU. In all three cases the temperature reaches 10^8 K before the onset of the next thermal pulse, so that all ^{13}C is consumed. In the FRANEC, MSSSP, and EVOL cases a typical interpulse period lasts for $\sim 40,000$, $\sim 50,000$, and $\sim 70,000$ yr, respectively (see Fig. 3). The time after the beginning of the interpulse period at which the temperature reaches 0.8×10^8 K is about 10,000 yr for the MSSSP and the FRANEC codes and 20,000 yr for EVOL. This is because the temperature in the MSSSP and FRANEC cases has been taken at a deeper, hence hotter, layer than in the EVOL case; however, it will not produce any important difference in the process of the neutron release. Since all ^{13}C is consumed, the total integrated neutron flux depends on the initial amount of ^{13}C and not on the way it burns. The neutron flux lasts for about 20,000 yr in the three cases, only
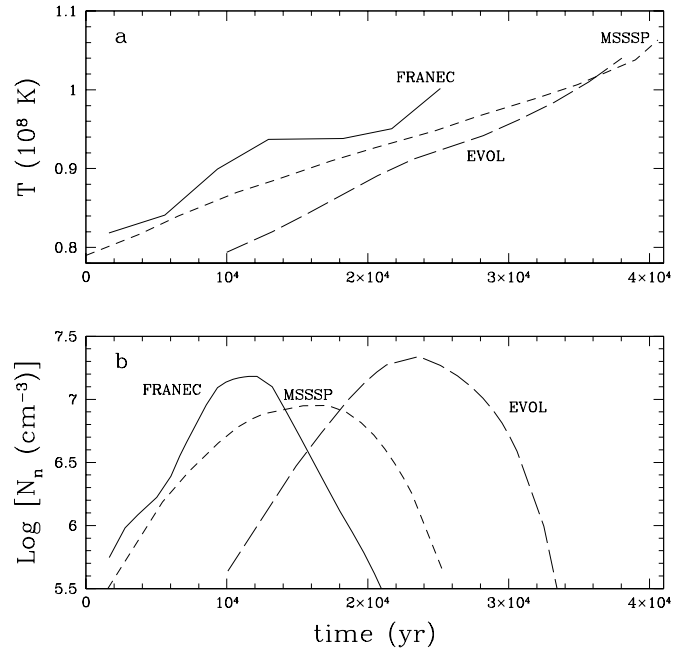
being shifted in time because of the different temperature trends. The neutron density peak reaches 1.5, 0.9, and 2.3×10^7 cm^{-3} using the FRANEC, MSSSP, and EVOL codes, respectively. These variations are unimportant, because the neutron density is too low in any case to affect any branching on the s-process path. Note that in the temperature range of interest, $T \simeq (0.8–1) \times 10^8$ K, the ^{13}C$(\alpha, n)^{16}$O rate we use is about 50%–70% lower than the one adopted in the NACRE compilation (Angulo et al. 1999). This difference would not make much change in the overall result. If ^{13}C burns faster, the maximum neutron density will be somewhat higher, yet still unimportant in affecting the s-abundances of branching-dependent isotopes.

In conclusion, the important difference among the three computations regarding the neutron flux in the ^{13}C pocket is the maximum neutron exposure reached within the region. As illustrated in detail in the previous sections, the maximum neutron exposure is doubled in the EVOL case with respect to the FRANEC and MSSSP cases, because intershell dredge-up in EVOL produces a double intershell abundance of ^{12}C. In the EVOL computation, the s-element distribution will be pushed toward heavy s-process elements.

3.4. The Neutron Flux in the Convective Regions by the ^{22}Ne Neutron Source

We mentioned in § 1 that ^{22}Ne is produced in the He intershell during the PDCZ by the ^{14}N$(\alpha, \gamma)^{18}$F$(\beta^+, \nu)^{18}$O$(\alpha, \gamma)^{22}$Ne chain that converts to ^{22}Ne all the ^{14}N significantly present in the ashes of the H burning and ingested in the PDCZ. The ^{14}N in the H ashes derives from the conversion of initial CNO nuclei; hence, it depends on the metallicity.
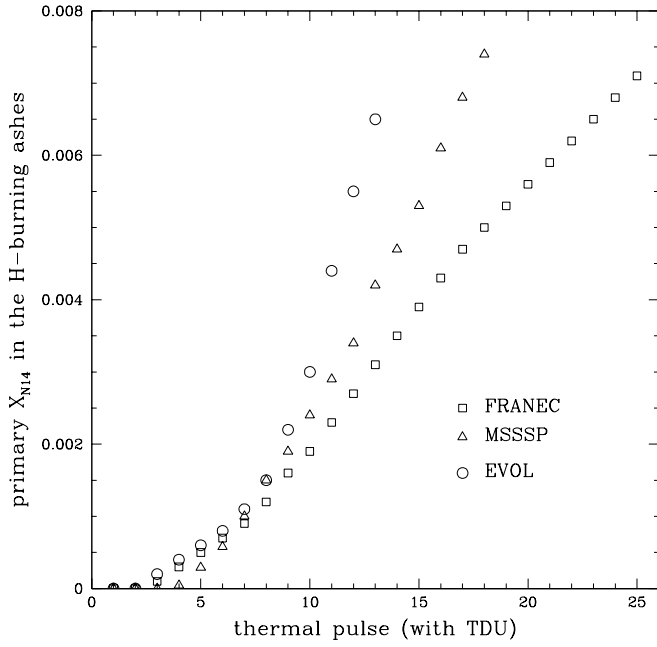
FIG. 8.—Primary contribution to the ^{14}N in the H-burning ashes as a function of thermal pulse number. Primary ^{14}N comes from the dredge-up of ^{12}C (and ^{16}O in the EVOL case) in the envelope, followed by H shell burning. To compute the total mass fraction of ^{14}N engulfed by each PDCZ, these values have to be added to the constant value of 0.0128 adopted in the *s*-process code for the H-burning ashes of solar metallicity.

FIG. 9.—(*a*) Temperatures at the bottom of the PDCZ and (*b*) neutron densities as functions of time during the last thermal pulse computed in three cases: the 25th with TDU for FRANEC (*solid lines*), the 18th with TDU for MSSSP (*short-dashed lines*), and the 13th with TDU for the EVOL code (*long-dashed lines*). The zero in time corresponds to the instant in which the bottom temperature in the convective shell reaches 2.5×10^8 K. Bottom densities decrease exponentially with time from $\sim 10^4$ to $\sim 10^3$ g cm^{-3}. The variation of temperature, matter density, and neutron density with pulse number for the FRANEC case can be found in Figs. 10, 11, and 13 of Gallino et al. (1998).

However, because primary ^{12}C (and also ^{16}O, if intershell dredge-up is at work) is dredged up from the He intershell in the envelope, the abundance of ^{14}N in the H ashes also contains a primary contribution that grows with the number and the strength of TDU episodes (Gallino et al. 1998). In Figure 8, we show the contribution of this primary component to the ^{14}N ingested in the PDCZs as computed by the different codes. In our computations the primary ^{14}N that is present in the ^{13}C pocket, as discussed in § 3.1, does not contribute significantly to the total ^{14}N ingested by the PDCZ, because the mass of the pocket is very small compared to the mass of the material processed by the H-burning shell (the typical ratio $M_{\text{pocket}}/\Delta M_{\text{H}}$ is around 1/15).

The *s*-process code activates the ^{22}Ne$(\alpha, n)^{25}$Mg reaction when the bottom temperature of the PDCZ grows above 2.5×10^8 K. We took the rate of the ^{22}Ne$(\alpha, n)^{25}$Mg reaction from Käppeler et al. (1994), excluding the elusive resonance at 633 keV and using the lower limit of the strength of the 828 keV resonance. In the temperature range of interest, $T \simeq (2–4) \times 10^8$ K, this rate is within a few percent of that adopted in the NACRE compilation (Angulo et al. 1999), while it is about 30% higher than the most recent determination, by Jaeger et al. (2001). Using this latest estimate would have a small effect on the results presented here, changing only little the abundances of the isotopes connected to the branching points that are very sensitive to the activation of the ^{22}Ne$(\alpha, n)^{25}$Mg reaction in the PDCZ, such as ^{96}Zr.

To compare the neutron fluxes during the thermal pulse, the first important parameter to consider is the maximum temperature at the bottom of each PDCZ. As shown in Figure 3, these temperatures, when computed by the FRANEC and MSSSP codes, are basically the same. A maximum temperature of $\simeq 3.05 \times 10^8$ K is found in the last PDCZ. With the EVOL code higher temperatures are achieved, as an
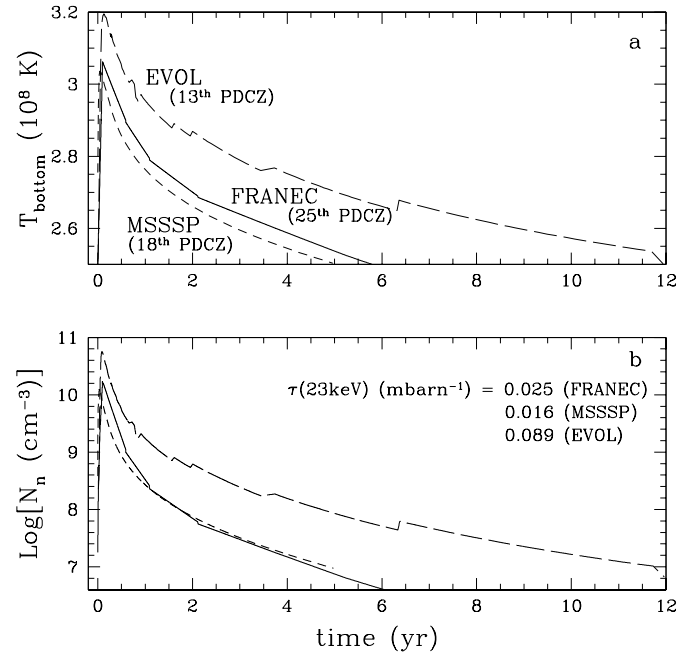
effect of the hydrodynamic overshoot applied at the base of the PDCZ, and the maximum reaches $\simeq 3.20 \times 10^8$ K. Hence, the ^{22}Ne$(\alpha, n)^{25}$Mg neutron source works more efficiently when the computation of the stellar evolution includes overshoot. Not only is the maximum temperature higher in this case, it is also high for a longer time, and the overall distributions in time of temperature and neutron density in a PDCZ change. This is illustrated in Figure 9, where we plot the bottom temperature trends for the last PDCZ computed by the three different stellar evolution calculations, together with the neutron densities computed by the *s*-process code on the basis of the three evolutionary codes. The temperature profile in the PDCZ has a narrow peak and hence, so does the neutron density. For the FRANEC and MSSSP computations the neutron exposures by the ^{22}Ne neutron burst are very small, about a factor of 20 smaller than those in the ^{13}C pocket. Note that this can be different for AGB star models of higher mass or of metallicity lower than solar ($Z < Z_\odot/2$), where the temperatures at the bottom of the PDCZs are higher (see, e.g., Lugaro et al. 1999). However, the neutron densities reach up to 10^{10} cm^{-3}, and branching points are extremely sensitive to this neutron flux (Gallino et al. 1998). In the EVOL case the neutron exposure in the PDCZs reaches almost 0.1 mbarn^{-1}, which is a value high enough to influence the production of the *s*-process elements of the Sr peak. Also, the neutron density is higher, up to about 6×10^{11} cm^{-3}; hence, we expect that in the EVOL computation, neutron-rich isotopes produced by branchings on the *s*-process path will be produced in greater amounts. An important example is ^{96}Zr: the

branching at the unstable ^{95}Zr is open when the neutron density is higher than $\simeq 5 \times 10^8$ cm^{-3}. From Figure 9, we see that this occurs for about a year in the FRANEC and MSSSP cases and for about 2 years in the case of the EVOL code. The tail of the temperature distribution is also important in determining some final abundances of isotopes involved in branchings because of the *freezeout* effect (Cosner, Iben, & Truran 1980). In any case, only a small amount of ^{22}Ne burns: for the PDCZs presented in Figure 9, 2.6%, 1.1%, and 8.9% of ^{22}Ne burns in the FRANEC, MSSSP, and EVOL cases, respectively.

3.5. *The Resulting s-Process Distributions*

In Figure 10, we show the production factors, with respect to solar abundances from Anders & Grevesse (1989), of the *s*-only isotopes in the He intershell material averaged over the dredged-up mass: $X_i^{\text{final}} = \sum_{j=1}^{N} X_i^j M_{\text{TDU}}^j / \sum_{j=1}^{N} M_{\text{TDU}}^j$. We sum over all TDU episodes, X_i^j is the abundance of the isotope i in the He intershell after the corresponding pulse with TDU j, and M_{TDU}^j is the mass dredged up. Also included are the production factors of ^{88}Sr, ^{138}Ba, and ^{208}Pb, representative of neutron magic nuclei at $N = 50$, 82, and 126, respectively, and of three neutron-rich nuclei most sensitive on branchings: ^{86}Kr, ^{87}Rb and ^{96}Zr. The *s*-process abundances approach an asymptotic distribution after about 5–10 TDU episodes. The production factors in the He intershell are up to a few hundreds and result in enhancements with respect to Fe of up to an order of magnitude in the envelope.

It has been noted in earlier studies, and pointed out again in recent work (see, e.g., Busso et al. 1999), that the *s*-process abundance distribution is grossly determined once the neutron capture cross sections and the total number of neutrons available are given. In other words, the neutron exposure determines the steps in the *s*-process abundance distribution at neutron magic nuclei and the slope of the
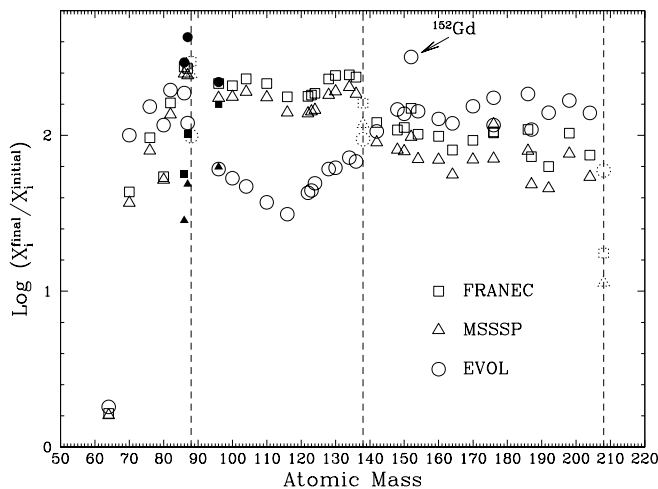

FIG. 10.—Distribution of production factors of *s*-only isotopes (*open symbols*) in the He intershell material, averaged over all TDU episodes and weighed by the mass dredged up (see text). The production factors of the neutron-rich isotopes ^{86}Kr, ^{87}Rb, and ^{96}Zr, which are affected by branchings, are also shown as filled symbols. The vertical lines are eye guides drawn at the stable neutron magic nuclei on the *s*-process path: ^{88}Sr, ^{138}Ba, and ^{208}Pb, whose production factors are also plotted using dashed symbols. The production factor of the *s*-only isotope ^{152}Gd is indicated by an arrow (see text for discussion).

distribution between the steps. This means that the general trends of the distributions shown in Figure 10 depend on the choice of the neutron exposures in the ^{13}C pocket. Although the FRANEC and MSSSP final distributions are very similar, since they use the same ^{13}C pocket, they show small differences: the more noticeable of these is that the production factors obtained with the MSSSP code are slightly lower than those obtained with the FRANEC code; moreover, the distributions are slightly different. This can be explained by the different structure inputs, mainly the mass of the convective regions, which is higher in the MSSSP case (see Fig. 3), resulting in a higher dilution of the material from the pocket in the He intershell.

For the EVOL case, the situation is different because of the higher neutron exposures in the ^{13}C pocket that are obtained as a result of the large abundance of ^{12}C in the He intershell produced by intershell dredge-up. While in the FRANEC and MSSSP cases the isotopes between the neutron magic nuclei ^{88}Sr and ^{138}Ba are more enhanced than the isotopes between the neutron magic nuclei ^{138}Ba and ^{208}Pb, the situation is reversed in the EVOL case because of the higher neutron exposures in the ^{13}C pocket. Also, at the very end of the *s*-process path, ^{208}Pb and ^{209}Bi are produced in much greater amounts in the EVOL case. As noted in § 3.4, in the EVOL case the neutron exposure in the PDCZs reaches 0.1 mbarn^{-1}, about 5 times more than the maximum value achieved with FRANEC and MSSSP. In this situation the abundances of isotopes with $70 \lesssim A \lesssim 100$ are mostly produced by the activation of the ^{22}Ne neutron source. In fact, a simulation of the EVOL case performed by excluding the ^{22}Ne neutron source gave production factors of 2, 15, and 30 for ^{70}Ge, ^{88}Sr, and ^{100}Ru, instead of 99, 96, and 50, respectively. Furthermore, the abundances of isotopes not affected by branching points from ^{138}Ba to ^{204}Pb were lower by about 50%, and the production factor of ^{208}Pb was lowered by a factor of 3. The distribution in the region between $100 \lesssim A \lesssim 138$, which is almost flat for FRANEC and MSSSP, is instead characterized in the EVOL case by a minimum at the *s*-only ^{116}Sn. Such a minimum is still present, but much less accentuated, in the simulation in which the ^{22}Ne neutron source was excluded.

The different modality of activation of the ^{22}Ne neutron source produces variations in the final results of isotopes involved in branchings. We include in Figure 10 the production factors of three interesting isotopes produced by branchings on the *s*-process paths: ^{86}Kr, which is sensitive to the branching at ^{85}Kr; ^{87}Rb, which is sensitive to the branchings at ^{85}Kr and ^{86}Rb; and ^{96}Zr, which is sensitive to the branching at ^{95}Zr. Because of the different neutron density profiles in the PDCZs (see Fig. 9), ^{86}Kr, ^{87}Rb, and ^{96}Zr are produced in much higher amounts in the EVOL computation. The fact that the MSSSP case produces less ^{86}Kr, ^{87}Rb, and ^{96}Zr with respect to the FRANEC case is due to the fact that the MSSSP model has fewer PDCZs with the highest temperature than the FRANEC, because of the effect of the higher mass-loss rate adopted.

Another interesting isotope is the *s*-only ^{152}Gd, whose production depends on the branching at ^{151}Sm. This isotope is actually positioned on the neutron-poor side of the branching, and hence it may be surprising that it is more produced in the EVOL case, which has the higher neutron density. However, this is explained by the freezeout effect: the abundances of isotopes connected with branching points freeze out at the time when "$\sigma \tau_{\text{rem}} \leq 1$, where σ is the

largest cross section involved in feeding the s-only isotope characterizing the branching and τ_{rem} is the remaining neutron exposure until the end of the pulse" (Käppeler et al. 1990). Hence, for higher σ, as in the case of the branching at ^{151}Sm, final abundances are determined late in the neutron flux, when the neutron density is low. The long tail of the neutron density distribution in the EVOL case (see Fig. 9) allows enough time for the isotopes connected to the "high-σ" branchings, such as ^{152}Gd, to determine most of their abundances at a late time during the neutron flux.

4. COMPARISON WITH OBSERVATIONAL CONSTRAINTS

From the earliest (Ulrich 1973; Iben 1975b) to more recent studies (Arlandini et al. 1999), a major constraint for the s-process in AGB stars has been the reproduction of the solar abundance distribution of the s-only nuclei belonging to the main component (i.e., the s-process isotopic distribution for atomic mass number $A > 90$). From Figure 10, it is clear that our resulting abundance distributions are nonsolar, since the production factors of s-only isotopes are not all the same. It has been already pointed out by Gallino et al. (1998), making use of the FRANEC code, that AGB stars of solar metallicity with our choice of the ^{13}C pocket do not reproduce the main component. We can extend this conclusion to the MSSSP and EVOL cases. However, since the abundance distribution mostly depends on the neutron exposures achieved in the ^{13}C pocket, which in turn depend on the ^{13}C amount (hence also on the intershell ^{12}C abundance) and, as previously discussed, on the stellar metallicity, roughly following the rule $\tau \sim {}^{13}\mathrm{C}/Z$ (Clayton 1988), we can obtain a best fit to the main component by adjusting these parameters. In the FRANEC and MSSSP cases, we need to produce more of the heavier elements beyond the step at ^{138}Ba, by increasing the neutron exposure by about a factor of 2. To accomplish this using the same ^{13}C pocket, we have to decrease the stellar metallicity to half solar (Gallino et al. 1998). For the EVOL case, on the other hand, we would need to decrease the neutron exposures in the ^{13}C pocket. We could try to accomplish this by using a smaller overshoot parameter at the base of the PDCZ and hence having a lower ^{12}C amount in the intershell, or by including some rotationally induced smearing, which would mix ^{14}N in the ^{13}C pocket during the interpulse, thus lowering the neutron exposure. In the EVOL case, however, we could still face great problems connected with the activation of the ^{22}Ne neutron source, such as the overproduction of ^{86}Kr, ^{87}Rb, ^{96}Zr, and ^{152}Gd.

However, we do not pursue this point, because "it is a basic premise of the Burbidge et al. (1957) theory of nucleosynthesis in stars" (Clayton et al. 1961) that solar abundances are expected to come not from a single star, but rather to be built up by Galactic chemical evolution. The more realistic approach to the origin of s-elements in the solar system has been presented by Travaglio et al. (1999, 2001) and involves the study of the Galactic chemical evolution of heavy elements, making use of yields from AGB stars of different masses and metallicities. Making use of the stellar yields computed with the FRANEC and s-process codes, these authors have shown that AGB stars of low mass can contribute satisfactorily to the Galactic abundances of the heavy s-elements. The roles of the s-process *weak component* from massive stars (Lamb et al. 1977; Raiteri, Gallino, &

Busso 1992) and of neutron capture nucleosynthesis in supernovae of Type II have to be reviewed in order to fully understand how many realistic contributions to the light s-elements up to $A \sim 90$ in the solar system are to be expected (Gallino et al. 2000).

Hence, we compare our model predictions with other observational constraints. Such comparison is not intended to be complete, since we are only considering one stellar model of given mass, metallicity, and ^{13}C pocket. We aim at understanding where the three different evolutionary sequences stand with respect to each other when related to observational constraints. The s-element enhancements at the stellar surface for AGB stars of solar metallicity are up to a factor of 10 (Busso et al. 2001), which is typically matched by our models after dilution of the He intershell material with the convective envelope. The logarithmic ratio with respect to solar [hs/ls], where "ls" is the average of light s-process elements (Y and Zr) and "hs" is the average of heavy s-process elements (Ba, La, Nd, and Sm), is a good indicator of the distribution of s-elements and varies in the range -0.6 to 0 for AGB stars of solar metallicity (Busso et al. 2001; Abia et al. 2002). The trends of our model predictions for [hs/ls] follow from what we observed in § 3.5: in the FRANEC and MSSSP cases, light s-process elements are more produced than heavy s-process elements and [hs/ls] is negative, while the opposite is true for EVOL. In that case, [hs/ls] ~ 0. In principle, stars with [hs/ls] ~ 0 cannot be covered by the FRANEC and MSSSP predictions at solar metallicity; however, they can fit into these models at slightly lower metallicities and hence are within observational uncertainties.

Together with spectroscopic observations of AGB stars, we also consider recent high-precision laboratory measurements of isotopic ratios of s-process elements in presolar silicon carbide grains (SiC; see review by Hoppe & Ott 1997). The vast majority (>90%) of SiC grains from the Murchison meteorite, the mainstream grains, most likely condensed in the mass-losing envelopes of carbon stars. Note that the condition $C/O > 1$ has to be satisfied for SiC molecules to condense. In particular, stars of low mass and around solar metallicity have been identified as the most likely parent stars of mainstream SiC (see Lugaro et al. 1999 for a thorough discussion). Measurements have been performed on aggregates of grains for Sr, Ba, Nd, Sm, and noble gases. Recently, a new technique, developed at the Fermi Institute of Chicago (Nicolussi et al. 1997), has allowed measurements of isotopic anomalies of Sr, Zr, Mo, and Ba in single SiC of the size of a few μm. The ratios ^{88}Sr/^{86}Sr and ^{138}Ba/^{136}Ba are sensitive to the neutron exposure. Measurements in aggregates of SiC grains indicate that, on average, the s-process distribution produced in SiC grain parent stars is accounted for by a nonsolar distribution produced by neutron fluxes in the pocket of about half the efficiency needed to reproduce the solar main component, such as that obtained in the FRANEC and MSSSP cases. The EVOL case produces instead too high ^{138}Ba/^{136}Ba and too low ^{88}Sr/^{86}Sr ratios. The ^{13}C pocket generated by the stellar model presented by Cristallo et al. (2001) has a neutron exposure profile with the same maximum s-process efficiency as we used in the FRANEC and MSSSP computations, $X_{\mathrm{C12}}^{\mathrm{intershell}} \sim 0.23$, but with a distribution in mass more weighted toward the regions with higher s-process efficiency. This results in an s-process distribution slightly pushed toward heavy s-elements, but little change in the

final results. The main difference is that the ^{88}Sr/^{86}Sr ratio increases going outside of the range observed in SiC.

All the above considerations, however, depend on the main model uncertainty: the ^{13}C pocket. For example, as mentioned above, making use of the FRANEC code, Busso et al. (2001) showed that one has to assume a spread in the ^{13}C pocket s-process efficiency to cover the range of spectroscopic observations at any metallicity. The same conclusion was reached by Lugaro et al. (2003) when considering single SiC grain data. It would be plausible to decrease the s-process efficiency in the pocket by means of stellar rotation, as shown by detailed modeling (Herwig et al. 2002), so that the effect of rotation may naturally explain the needed spread of ^{13}C pocket efficiencies at each metallicity. This effect would also lower the neutron exposure in the pocket found by EVOL.

Let us consider a few observational constraints that are sensitive to the high neutron exposure deriving from the activation of the ^{22}Ne in the PDCZ. The high efficiency of the ^{22}Ne neutron source produces in EVOL a situation similar to that occurring in intermediate-mass and low-metallicity stars. The fact that overshoot at the base of the PDCZ induces a higher occurrence of α captures on ^{22}Ne is in contrast with spectroscopic observations of Mg, which have shown that Mg isotopes are present in solar proportion in AGB stars of about solar metallicity (Clegg, Lambert, & Bell 1979; Smith & Lambert 1986). In the FRANEC and MSSSP cases, we have a modest increase of the ^{25}Mg/^{24}Mg and ^{26}Mg/^{24}Mg ratios in the envelope, from the solar values of 0.13 and 0.14, respectively, to about 0.16. In the EVOL case these ratios increase more abruptly, up to values around 0.45 (see also Herwig 2000). The [Rb/Sr] ratio in AGB stars is typically negative (Lambert et al. 1995; Abia et al. 2001). In the FRANEC and MSSSP cases the [Rb/Sr] ratio is always negative, while in the EVOL case it is always positive, at odds with observations. Large depletions of ^{96}Zr/^{94}Zr are seen in single SiC (Nicolussi et al. 1997), indicating that neutron densities in the stellar sources of these grains must have been low. These measurements are compatible with the FRANEC and MSSSP cases. The EVOL model produces instead only large positive values of the ^{96}Zr/^{94}Zr ratio. All these effects depend on the choice of the free parameter f at the base of the PDCZ.

5. CONCLUSIONS

We presented detailed computations of the s-process abundance distribution of heavy elements for a 3 $M_\odot$ star of solar metallicity, making use of three different evolutionary codes. One of them includes a time-dependent hydrodynamic overshoot mechanism and finds the ^{13}C pocket self-consistently. A hydrodynamic overshoot mechanism at the base of the convective envelope is a likely process to produce a ^{13}C pocket. The alternative mixing process related to rotation may limit the neutron flux by continued mixing of ^{14}N into the s-process layer during the interpulse phase (Herwig et al. 2002). A combination of both processes should be

investigated in the future. It is, of course, conceivable that other mixing processes could be involved that may have complementary or similar properties to those of the hydrodynamic overshoot mechanism considered here. Overshoot at the base of the convective envelope generates higher TDU efficiencies, making it possible to create carbon stars at very low luminosities. The inclusion of overshoot at the base of the PDCZ and the consequent intershell dredge-up help to explain the observed carbon and oxygen abundances of H-deficient central stars of planetary nebulae.

The two computations that do not include overshoot do not self-consistently find any proton diffusion at the end of TDU, and we assumed an identical ^{13}C pocket for these cases. The final results of these two cases are remarkably similar, and we can conclude that the main uncertainty in s-process predictions is the ^{13}C pocket and not the intrinsic differences among different codes when no overshoot mechanism is included. In the case that includes hydrodynamic overshoot, because of penetration of the intershell convective region into the C-O core, (1) the abundance of ^{12}C in the intershell and hence the maximum total neutron exposure achieved in the ^{13}C pocket are higher than in the other cases, and (2) the neutron flux in the PDCZs is stronger. In summary, overshoot at the base of the convective envelope produces a ^{13}C pocket if large efficiencies, i.e., values of the parameter f, are assumed; overshoot at the base of the PDCZ influences the activation of the ^{13}C$(\alpha, n)^{16}$O and ^{22}Ne$(\alpha, n)^{25}$Mg neutron sources, producing a more efficient neutron flux in both situations. The final resulting abundance distributions of heavy elements reflect such features of the neutron fluxes: in the case with overshoot included, the heaviest elements, such as Sm, are produced in greater amounts than lighter elements, such as Sn. At the end of the s-process path ^{208}Pb is produced in a higher amount, as are also isotopes fed by branching points, such as ^{86}Kr, ^{87}Rb, and ^{96}Zr.

With our choice of the ^{13}C pocket profile, the results from the two cases without overshoot give a good match to several observational constraints. The strong intershell dredge-up connected with overshoot at the base of the PDCZs is in several situations in contrast with observational constraints. We still need to expand this study to a range of masses and metallicities. Within the EVOL case, we also need to extend our calculations in the space of the free overshoot parameter f, as applied at different boundaries and possibly also different times during the evolution, in order to test which range of f could provide us with the closest match to observational constraints. For example, a preliminary test with $f = 0.008$ applied at the base of the PDCZ show a significantly reduced efficiency in the activation of the ^{22}Ne neutron source.

REFERENCES

Abia, C., Busso, M., Gallino, R., Domínguez, I., Straniero, O., & Isern, J. 2001, ApJ, 559, 1117
Abia, C., et al. 2002, ApJ, 579, 817
Anders, E., & Grevesse, N. 1989, Geochim. Cosmochim. Acta, 53, 197
Angulo, C., et al. 1999, Nucl. Phys. A, 656, 3
Arlandini, C., Käppeler, F., Wisshak, K., Gallino, R., Lugaro, M., Busso, M., & Straniero, O. 1999, ApJ, 525, 886

Arndt, T. U., Fleischer, A. J., & Sedlmayr, E. 1997, A&A, 327, 614
Asida, S. M., & Arnett, D. 2000, ApJ, 545, 435
Bao, Z. Y., Beer, H., Käppeler, F., Voss, F., Wisshak, K., & Rauscher, T. 2000, At. Data Nucl. Data Tables, 76, 70
Becker, S. A., & Iben, I., Jr. 1979, ApJ, 232, 831
Blöcker, T. 1995, A&A, 297, 727
Boothroyd, A. I., & Sackmann, I.-J. 1988a, ApJ, 328, 632

Boothroyd, A. I., & Sackmann, I.-J. 1988b, ApJ, 328, 641
———. 1988c, ApJ, 328, 653
———. 1988d, ApJ, 328, 671
Burbidge, E. M., Burbidge, G. R., Fowler, W. A., & Hoyle, F. 1957, Rev. Mod. Phys., 29, 547
Busso, M., Gallino, R., Lambert, D. L., Travaglio, C., & Smith, V. V. 2001, ApJ, 557, 802
Busso, M., Gallino, R., & Wasserburg, G. J. 1999, ARA&A, 37, 239
Castellani, V., Chieffi, A., & Straniero, O. 1990, ApJS, 74, 463
Castellani, V., Giannone, P., & Renzini, A. 1971, Ap&SS, 10, 340
Caughlan, G. R., & Fowler, W. A. 1988, At. Data Nucl. Data Tables, 40, 283
Chieffi, A., Domínguez, I., Limongi, M., & Straniero, O. 2001, ApJ, 554, 1159
Clayton, D. D. 1968, Principles of Stellar Evolution and Nucleosynthesis (Chicago: Univ. Chicago Press)
———. 1988, MNRAS, 234, 1
Clayton, D. D., Fowler, W. A., Hull, T. E., & Zimmerman, B. A. 1961, Ann. Phys., 12, 331
Clayton, D. D., & Rassbach, M. E. 1967, ApJ, 148, 69
Clegg, R. E. S., Lambert, D. L., & Bell, R. A. 1979, ApJ, 234, 188
Cosner, K., Iben, I., Jr., & Truran, J. W. 1980, ApJ, 238, L91
Cristallo, S., Straniero, O., Gallino, R., Herwig, F., Chieffi, A., Limongi, M., & Busso, M. 2001, Nucl. Phys. A, 688, 217
Denissenkov, P. A., & Tout, C. A. 2003, MNRAS, in press
Denker, A., et al. 1995, in AIP Conf. Proc. 327, Nuclei in the Cosmos III, ed. M. Busso, R. Gallino, & C. M. Raiteri (New York: AIP), 255
Dreizler, S., & Heber, U. 1998, A&A, 334, 618
Forestini, M., & Charbonnel, C. 1997, A&AS, 123, 241
Freytag, B., Ludwig, H.-G., & Steffen, M. 1996, A&A, 313, 497
Frost, C. A., & Lattanzio, J. C. 1996, ApJ, 473, 383
Gallino, R., Arlandini, C., Busso, M., Lugaro, M., Travaglio, C., Straniero, O., Chieffi, A., & Limongi, M. 1998, ApJ, 497, 388
Gallino, R., Busso, M., Lugaro, M., Straniero, O., Käppeler, F., & Arlandini, C. 2000, Mem. Soc. Astron. Italiana, 71, 771
Gallino, R., Busso, M., Picchio, G., Raiteri, C. M., & Renzini, A. 1988, ApJ, 334, L45
Gledenov, Yu. M., Salatski, V. I., Sedyshev, P. V., Sedysheva, M. V., Koehler, P. E., Vesna, V. A., & Okunev, I. S. 1995, in AIP Conf. Proc. 327, Nuclei in the Cosmos III, ed. M. Busso, R. Gallino, & C. M. Raiteri (New York: AIP), 173
Goriely, S., & Mowlavi, N. 2000, A&A, 362, 599
Groenewegen, M. A. T., van den Hoek, L. B., & de Jong, T. 1995, A&A, 293, 381
Herwig, F. 2000, A&A, 360, 952
Herwig, F., Blöcker, T., & Driebe, T. 2000, Mem. Soc. Astron. Italiana, 71, 745
Herwig, F., Blöcker, T., Langer, N., & Driebe, T. 1999, A&A, 349, L5
Herwig, F., Blöcker, T., Schönberner, D., & El Eid, M. 1997, A&A, 324, L81
Herwig, F., Langer, N., & Lugaro, M. 2002, in IAU Symp. 209, Planetary Nebulae: Their Evolution and Role in the Universe, ed. M. Dopita et al. (San Francisco: ASP), in press (astro-ph/0202067)
Herwig, F., Schönberner, D., & Blöcker, T. 1998, A&A, 340, L43
Hollowell, D., & Iben, I., Jr. 1988, ApJ, 333, L25
Hoppe, P., & Ott, U. 1997, in AIP Conf. Proc. 402, Astrophysical Implications of the Laboratory Study of Presolar Materials, ed. T. Bernatowicz & E. Zinner (New York: AIP), 27
Iben, I., Jr. 1975a, ApJ, 196, 525
———. 1975b, ApJ, 196, 549
———. 1976, ApJ, 208, 165
Iben, I., Jr., & Renzini, A. 1982a, ApJ, 259, L79
———. 1982b, ApJ, 263, L23
Jaeger, M., Kunz, R., Mayer, A., Hammer, J. W., Staudt, G., Kratz, K. L., & Pfeiffer, B. 2001, Phys. Rev. Lett., 87, 202501
Jorissen, A., & Arnould, M. 1989, A&A, 221, 161
Käppeler, F., Beer, H., & Wisshak, K. 1989, Rep. Prog. Phys., 52, 945
Käppeler, F., Gallino, R., Busso, M., Picchio, G., & Raiteri, C. M. 1990, ApJ, 354, 630

Käppeler, F., et al. 1994, ApJ, 437, 396
King, J. D., Azuma, R. E., Vise, J. B., Görres, J., Rolfs, C., Trautvetter, H. P., & Vlieks, A. E. 1994, Nucl. Phys. A, 567, 354
Lamb, S. A., Howard, W. M., Truran, W. A., & Iben, I., Jr. 1977, ApJ, 217, 213
Lambert, D. L., Smith, V. V., Busso, M., Gallino, R., & Straniero, O. 1995, ApJ, 450, 302
Langer, N., Heger, A., Wellstein, S., & Herwig, F. 1999, A&A, 346, L37
Lattanzio, J. C. 1986, ApJ, 311, 708
———. 1987, ApJ, 313, L15
———. 1989, ApJ, 344, L25
Leuenhagen, U., & Hamann, W.-R. 1998, A&A, 330, 265
Lugaro, M. 1998, in Nuclei in the Cosmos V, ed. N. Prantzos & S. Harissopoulos (Gif-sur-Yvette: Editions Frontières), 501
Lugaro, M., Davis, A. M., Gallino, R., Pellin, M. J., Straniero, O., & Käppeler, F. 2003, ApJ, submitted
Lugaro, M., & Herwig, F. 2001, Nucl. Phys. A, 688, 201
Lugaro, M., Zinner, E., Gallino, R., & Amari, S. 1999, ApJ, 527, 369
Marigo, P. 2002, A&A, 387, 507
Mazzitelli, I., D'Antona, F., & Ventura, P. 1999, A&A, 348, 846
Mowlavi, N. 1999, A&A, 344, 617
Mutti, P., Beer, H., Brusegan, A., & Corvi, F. 2002, in J. Nucl. Sci. Tech. Suppl. 2, 569
Nicolussi, G. K., Davis, A. M., Pellin, M. J., Lewis, R. S., Clayton, R. N., & Amari, S. 1997, Science, 277, 1281
Olofsson, H., González Delgado, D., Kerschbaum, F., & Schöier, F. L. 2002, A&A, 391, 1053
Paczyński, B. 1970, Acta Astron., 20, 47
———. 1974, ApJ, 192, 483
Pols, O. R., & Tout, C. A. 2001, Mem. Soc. Astron. Italiana, 72, 299
Raiteri, C. M., Gallino, R., & Busso, M. 1992, ApJ, 387, 263
Reifarth, R., Käppeler, F., Voss, F., & Wisshak, K. 2001, Nucl. Phys. A, 688, 229
Reimers, D. 1975, in Problems in Stellar Atmospheres and Envelopes, ed. B. Baschek, W. H. Kegel, & G. Traving (New York: Springer), 229
Schaller, G., Schaerer, D., Meynet, G., & Maeder, A. 1992, A&AS, 96, 269
Schlattl, H., & Weiss, A. 1999, A&A, 347, 272
Schönberner, D. 1979, A&A, 79, 108
Schwarzschild, M., & Härm, R. 1965, ApJ, 142, 855
Singh, H. P., Roxburgh, I. W., & Chan, K. L. 1998, A&A, 340, 178
Smith, V. V., & Lambert, D. L. 1986, ApJ, 311, 843
———. 1990, ApJS, 72, 387
Straniero, O., Chieffi, A., Limongi, M., Busso, M., Gallino, R., & Arlandini, C. 1997, ApJ, 478, 332
Straniero, O., Gallino, R., Busso, M., Chieffi, A., Raiteri, C. M., Salaris, M., & Limongi, M. 1995, ApJ, 440, L85
Takahashi, K., & Yokoi, K. 1987, At. Data Nucl. Data Tables, 36, 375
Thielemann, F.-K., Arnould, M., & Truran, J. W. 1987, in Proc. 2d IAP Workshop: Advances in Nuclear Astrophysics, ed. E. Vangioni-Flam, J. Audouze, M. Cassé, J. P. Chièze, & J. Trân Thanh Vân (Gif-sur-Yvette: Editions Frontières), 525
Travaglio, C., Galli, D., Gallino, R., Busso, M., Ferrini, F., & Straniero, O. 1999, ApJ, 521, 691
Travaglio, C., Gallino, R., Busso, M., & Gratton, R. 2001, ApJ, 549, 346
Ulrich, R. K. 1973, in Explosive Nucleosynthesis, ed. D. N. Schramm & W. D. Arnett (Austin: Univ. Texas Press), 139
Vassiliadis, E., & Wood, P. R. 1993, ApJ, 413, 641
Wachter, A., Schröder, K.-P., Winters, J. M., Arndt, T. U., & Sedlmayr, E. 2002, A&A, 384, 452
Wagenhuber, J., & Groenewegen, M. A. T. 1998, A&A, 340, 183
Wallerstein, G., & Knapp, G. R. 1998, ARA&A, 36, 369
Wallerstein, G., et al. 1997, Rev. Mod. Phys., 69, 995
Ward, R. A., Newman, M. J., & Clayton, D. D. 1976, ApJS, 31, 33
Wood, P. R. 1981, in Physical Processes in Red Giants, ed. I. Iben, Jr. & A. Renzini (Dordrecht: Reidel), 135
Wood, P. R., & Zarro, D. M. 1981, ApJ, 247, 247